JOURNAL OF GEOPHYSICAL RESEARCH, VOL. 116, B06309, doi:10.1029/2010JB007721, 2011

Origin of pulverized rocks during earthquake fault rupture

Fuping Yuan,[1,2] Vikas Prakash,[1] and Terry Tullis[3]

Received 27 May 2010; revised 4 January 2011; accepted 22 March 2011; published 24 June 2011.

[1] The origin of pulverized rocks (PR) in surface outcrops adjacent to the fault cores of the San Andreas and other major faults in Southern California is not clear, but their structural context indicates that they are clearly associated with faulting. An understanding of their origin might allow inferences to be drawn about the nature of dynamic slip on faults, including rupture mechanisms and their speed during earthquakes. In the present study, we use split Hopkinson bar recovery experiments to investigate whether PR can be produced under dynamic stress wave loading conditions in the laboratory and whether PR is diagnostic of any particular process of formation. The results of the study indicate that in Westerly granite for transition from sparse fracture to pervasive pulverization requires high strain rates in excess of 250/s and that the formation of PR may be inhibited at the larger burial depths. The constraint imposed by field observations of the relatively low strains (1–3%) in PR recovered from the field and the laboratory derived threshold for the critical strain rate (~250/s and higher) together indicate that a dynamic supershear-type rupture may be necessary for the origin of pulverized rocks at distances of tens of meters away from the fault plane as observed in the field for both large strike-slip-type and the relatively small dip-slip-type fault ruptures in nature.

Citation: Yuan, F., V. Prakash, and T. Tullis (2011), Origin of pulverized rocks during earthquake fault rupture, *J. Geophys. Res.*, *116*, B06309, doi:10.1029/2010JB007721.

1. Introduction

[2] Geological mapping indicates that fault zones contain a hierarchical damage structure with a narrow core of slip localization that accommodates most of the motion across the fault and damaged rocks with various crack densities in the adjacent regions [*Chester et al.*, 2004]. Recent studies [*Dor*, 2006, 2007; *Dor et al.*, 2006b, 2006c, 2009; *Reches and Dewers*, 2004, 2005; *Wilson et al.*, 2004, 2005] have shown that large continental strike-slip fault structures have belts of pulverized rocks (PR) that are about 100 to 300 m wide and exist primarily on one side of the fault. A principal feature exhibited by PR is that they appear to be essentially shattered in place but have experienced very little strain; the PR consists of fragments much smaller than the original crystal/grain size of the intact rock. These fragments still fit together, essentially preserving the original rock fabric on all scales.

[3] PR have been found to be a systematic structural component of the San Andreas Fault (SAF) zone in the Mojave segment [*Dor et al.*, 2006b; *Wilson et al.*, 2005], portions of the Garlock [*Sisk et al.*, 2005] and San Jacinto faults [*Stillings*, 2007] in California, and in a section of the Arima-Takatsuki fault in Japan [*Mitchell et al.*, 2008]. What is intriguing is the fact that such distributions of intensely fragmented rocks at distance of tens of meters away from the fault plane are rarely observed on other natural faults, in which the damage is usually localized along macroscopic principal shear planes.

[4] Following several observations of PR along the SAF, *Brune* [2001], *Wilson et al.* [2005], and *Rockwell et al.* [2009] have studied in detail an outcrop of the pulverized Tejon Lookout granite in the Tejon Pass and from the Tejon Ranch on the Garlock fault [*Sisk et al.*, 2005]. Based on the analysis of particle size distributions (PSD) they argued that the energy dissipated during fracturing (and/or energy required to create the extremely fine grain gouge) may be considerably larger than prior estimates, and thus may have implications to the overall earthquake energy budget. To verify whether the observed occurrence of PR along the Mojave section of the SAF was anecdotal or systematic, *Dor et al.* [2006b] mapped all the outcrops of crystalline rocks along this fault section. The damage pattern (PR) was observed to be present mainly in the crystalline rock that was not extensively weathered and had only a minor clay content. They also found that essentially every outcrop of crystalline rock within 50 to 200 m from the fault was pulverized to some degree, suggesting that PR were a systematic fault zone damage product. Moreover, the PR layer was observed to be parallel to the slipping zone of the fault and apparently shifted to the northeast. *Dor et al.* [2006a, 2006b] suggested this asymmetry could be due to the propagation of wrinkle-like ruptures along a bimaterial interface [*Ben-Zion and Shi*, 2005] with a preferred northwest propagation direction of

---

[1] Department of Mechanical and Aerospace Engineering, Case Western Reserve University, Cleveland, Ohio, USA.

[2] State Key Laboratory of Nonlinear Mechanics, Institute of Mechanics, Chinese Academy of Sciences, Beijing, China.

[3] Department of Geological Sciences, Brown University, Providence, Rhode Island, USA.

0148-0227/11/2010JB007721

large earthquakes on the Mojave section of the fault. *Dor et al.* [2006a, 2006b] also argued that pulverization occurred in a shallow zone in the crust, probably at the top 3 km. This conclusion was further substantiated by the finding of significant amounts of similar type of damage in sandstones of the Juniper Hills formation [*Dor et al.*, 2009] in a 100 m wide zone adjacent to the SAF. These rocks were not buried deeply, and the structural context of their damage suggests that it was related to faulting on the SAF. *Dor* [2007] also analyzed PSD of samples collected from the Mojave section of the SAF by scanning electron microscope. Their results showed a distribution of particle diameters between 0.4 to 100 μm, i.e., much smaller than the grain size of the rocks.

[5] With regards to the origin of PR, it has been argued that since faults show varying degrees of amplitude-to-wavelength (surface roughness) ratios [*Power and Tullis*, 1989, 1995; *Power et al.*, 1988; *Yund et al.*, 1990], pulverization of rocks may occur during slip on a rough fault surface, where the material on the fault surface may repeatedly experience a variety of strain orientations, mainly extensions and compressions perpendicular to the main fault surface. Similarly, *Chester and Chester* [2000] have postulated that locally inhomogeneous stress states can occur along faults owing to repeated (cyclic) slip on geometrically irregular fault surfaces, thus leading to an increase in the variation in both principal stress orientation and magnitude along the fault surface, and the likelihood for brittle failure. In these models, pulverization of rocks occurs simply due to the irregular geometry of the fault surface and may not require any high strain rates.

[6] In contrast to the above scenario, another class of models emphasizes the association of the rupture tip with fault interface vibrations leading in some cases to a complete reduction of the normal stress. The difference lies in the fact that fault roughness is intrinsically a part of the model, unlike the idealized planar fault in the aforementioned rupture model. Thus, a given point along a fault experiences not only a complex and rapidly evolving stress state as the rupture tip passes, but continues to experience significant stress changes behind the rupture tip as long as slip is occurring, and may lead to fragmentation in the adjoining rock. This model was suggested, among others, by the experiments and calculations of Brune and coworkers [e.g., *Brune et al.*, 1993], by the 2D finite element modeling of *Oglesby et al.* [1998, 2000], and by the theory of rupture along a bimaterial interface [e.g., *Ben-Zion*, 2001; *Lyakhovsky et al.*, 2001].

[7] Another possibility for the pulverization of the rock can be attributed to the damage from stress waves associated with the passage of a dynamic shear rupture tip propagating at sub-Rayleigh and/or intersonic speeds. Under these dynamic loading conditions formation of a single dominant crack and/or multiple sparsely spaced dominant macrocracks is limited by the Rayleigh wave speed of the medium and, thus, cannot accommodate all the energy provided. Instead, the dynamic loading invariably results in nucleation and propagation of numerous densely spaced microcracks, which ultimately coalesce, leading to fragmentation and, possibly, complete pulverization of the sample [*Freund*, 1990]. This damage may occur even in the case of an ideally planar fault, during a single rupture event or many times over as ruptures from successive earthquakes pass by. The orientation of the dynamic stresses at a given point varies during the passage of the rupture tip. The largest stresses occur immediately ahead of the tip and in the process zone immediately behind it. The dimensions of the process zone could be as large as 30 m if the slip weakening distance is on the order of 50 mm [*Templeton and Rice*, 2008; *Viesca et al.*, 2008], and so, with a rupture speed on the order of the shear wave speed in the material (~3 km/s), a material point experiences these changing stresses for about 0.01 s (~30 m divided by 3 km/s). The magnitude of the stress involved in this situation is expected to be on the order of the Coulomb failure stress, but the amplitude of the permanent strain is expected to be small, on the order of 0.5 percent [*Templeton and Rice*, 2008]. Along these lines, deformation conditions at the tip of a propagating dynamic rupture can be expected to cause pervasive fragmentation of brittle solids and/or granular materials.

[8] In addition to the change in orientation and magnitude of the principal stresses, elastodynamic crack tip fields during Mode II rupture also indicate that very high rates of volumetric expansion and/or contraction exist at short distances from the tip of such dynamic ruptures. As the tip approaches a material point in the fault zone, volumetric deformation rates intensify and can lead to fragmentation of the solid rock. As the rupture tip passes by the material point, the volumetric expansion is inverted, leading to further fragmentation of the newly formed granular material by dynamic contraction. Such stress wave loading conditions have been suggested by *Reches and Dewers* [2005] and *Grady and Kipp* [1993] to aid in rock fragmentation during the passage of a dynamic shear rupture front.

[9] Despite the above efforts, the origin of PR at distances of tens of meters away from the fault plane is still not clear. Whereas grain comminution and gouge formation are common within the fault core, (where much of the straining occurs), the combination of intense pulverization with the apparent lack of significant strain suggests that they have the potential for telling us something new about the faulting process and, if generated by earthquakes, about the dynamics of rupture events. In particular, the governing elastodynamic equations for Mode II shear rupture predict high volumetric and/or effective strain rates at material elements very close to the fault core, but relatively smaller strain rates at distances several tens of meters away. If the effective strain rate threshold for pulverization of the rocks is high, it may suggest that perhaps pulverization may be related to supershear rupture, a type of dynamic shear rupture only detected infrequently, which is associated with a shock wave [*Doan and Gary*, 2008, 2009; *Prakash et al.*, 2008; *Yuan and Prakash*, 2009]. This hypothesis is also consistent with the fact that pulverization has been observed along large strike-slip faults, such as, the San Andreas Fault in CA and the North Anatolian Fault in Turkey. These faults are known to be prone to supershear rupture [*Rosakis*, 2002; *Rosakis et al.*, 2009].

[10] The present experimental study is motivated by the need to better understand the critical stress wave loading conditions (effective strain rate and stress amplitude) that may be required for a transition in failure in rocks from discrete fracturing to pervasive pulverization of the type observed in PR. In the study we employ split Hopkinson pressure bar (SHPB) recovery experiments on Westerly

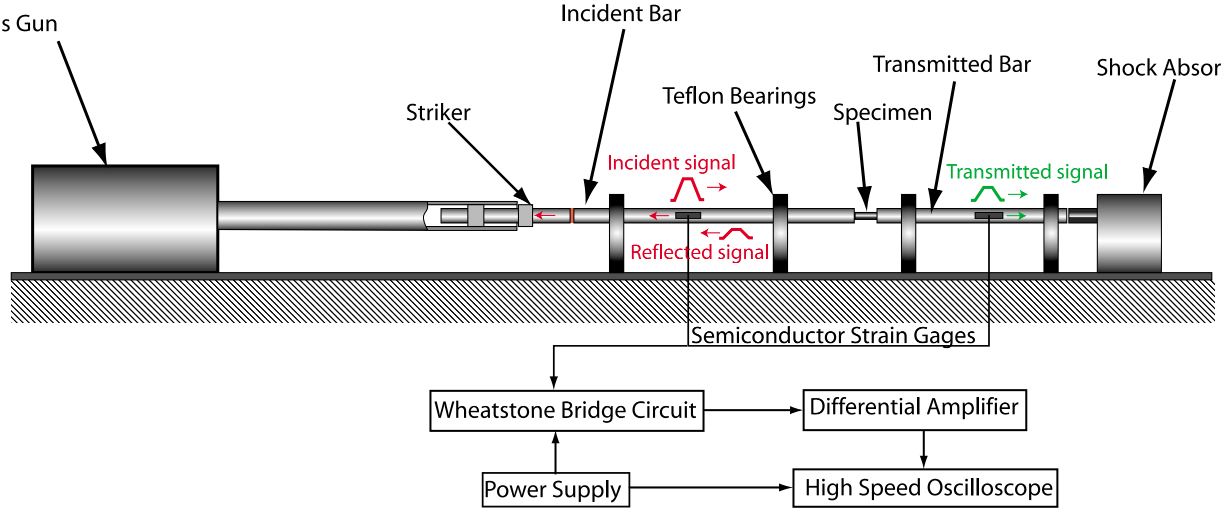

Figure 1. Schematic of the Split-Hopkinson Pressure Bar used in conducting the recovery experiments on Westerly granite.

granite samples in both unconfined (uniaxial) and confined conditions. The SHPB technique provides average stress, strain, and strain rate in the sample under various load confinement conditions at strain rates in excess of 1000 s^{-1}. We also employ detailed optical and scanning electron microscopy to delineate the various damage modes and failure in the posttest impacted granite samples. Details of the experimental technique are provided next in Section 2.0.

2. Experimental Procedure

[11] In the present study, a modified Split-Hopkinson Pressure Bar (SHPB) with a single stress wave loading capability for recovery purposes [*Chen and Ravichandran*, 1997] was employed to conduct the high strain rate experiments on Westerly granite. A schematic of the SHPB facility, located in the Department of Mechanical and Aerospace Engineering at Case Western Reserve University. is shown in Figure 1. The loading device consists of a pressurized gas gun and three 19.05 mm diameter maraging steel bars − 0.1/0.2 m long striker bar (propelled by the gas gun), 1.6 m incident bar, and an 0.8 m transmitter bar. The specimen is placed between the incident and transmitter bars prior to the experiment. Upon impact of the striker bar with the incident bar, compressive stress waves are generated in the incident and striker bars. When the stress wave in the incident bar reaches the specimen–incident bar interface, part of the incident stress wave is reflected back in the incident bar as an unloading wave while the rest continues through to the transmitter bar. Semiconductor strain gages are mounted on the incident and transmitter bars to record the strain profile histories generated by the impact; these gauges are mounted diametrically opposite each other to minimize the effects due to bending.

[12] In the conventional split Hopkinson pressure bar, it is possible that the specimen is loaded multiple times because of subsequent wave reflections in the incident bar. This repeated loading is undesirable to enable investigation of the critical conditions for pulverization of the rock specimens under well-characterized stress wave loading conditions. In order to achieve this, in the present study, the transmitter bar was made to be shorter than the incident bar, as shown in the Figure 1. With this modification, the shorter transmitter bar acts as a momentum trap, thereby moving the transmitter bar away from the specimen before the second compressive loading pulse reaches the specimen.

[13] As pointed out by *Davies and Hunter* [1963], in a typical split Hopkinson bar test the stress state within the specimen equilibrates after approximately π reverberations of the stress pulse within the specimen:

$$t_{equil} = \frac{\pi L_o}{c_{granite}} \tag{1}$$

where L_o is the specimen length and $c_{granite}$ is the longitudinal wave speed in Westerly granite. Based on the available literature [*Ashby and Sammis*, 1990; *Hadley*, 1976; *Lockner*, 1998; *Schock and Heard*, 1974] Westerly granite has an average Young's modulus of 70 GPa and an approximate density of 2650 kg/m^3. These values give a longitudinal elastic bar wave speed of approximately 5.1 km/s in the granite. In view of equation (1), for the 7 mm thick Westerly granite used in the present study, the stresses are expected to reach an equilibrium after approximately 5 μs. In order to facilitate the attainment of stress equilibrium, and thus a nearly constant strain rate in the sample during the duration of the experiment, a pulse shaper is placed at the impact end (left end) of the incident bar to shape (increase) the risetime of the incident pulse by plastic flow of the pulse shaper [*Shazly et al.*, 2009; *Sunny et al.*, 2008]. In this way, the times at which the peak stress occurs in the granite specimens will always be greater than those required to reach an equilibrium state of stress in the specimens. In view of this, in all the tests conducted in present study, annealed copper shims of various sizes were used as the pulse shapers [*Frew et al.*, 2002]. The size of the shims depend on the impact velocity to be used in the experiment, and were optimized by matching the slopes of the incident signals (resulting from impacting the incident bar with different pulse shapers

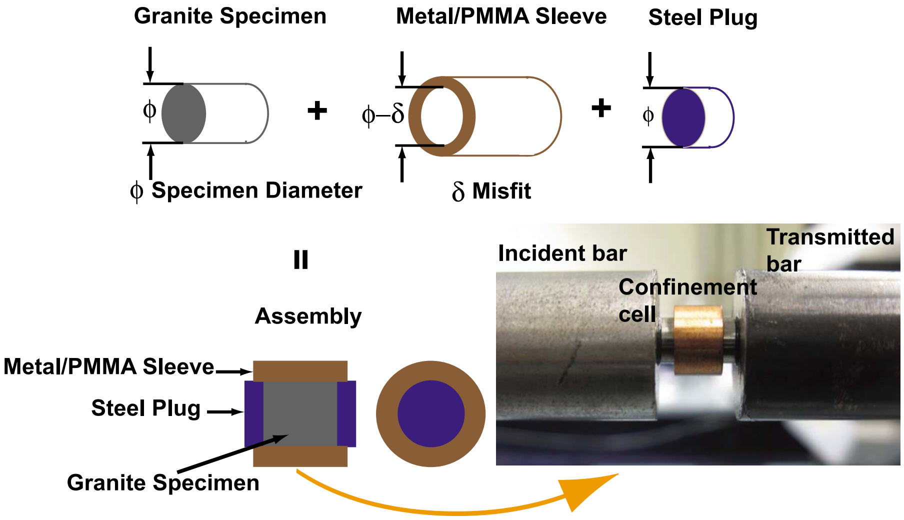

Figure 2. Schematic of confinement cell assembly used for conducting the confined SHPB experiments.

placed between the incident and striker bars) with the transmitted signal.

[14] The lateral confinement in the rock samples was achieved by installing a shrink fit PMMA/metal sleeve on the lateral surface of the cylindrical Westerly granite specimens. A typical confinement cell assembly with copper sleeve is shown in Figure 2. The inner diameter of the sleeve was designed to be slightly smaller than the specimen diameter (a misfit is applied). To install the sleeve around the specimen, the sleeve is preheated to expand the inner diameter and enable the specimen to slide into the sleeve. After the assembly is cooled, shrinkage of the sleeve provides confinement pressure on the lateral surface of the specimen. The initial misfit is chosen to be large enough so as to take the sleeve into the plastic regime during the shrinkage. In the case of relatively thin-walled sleeves, the lateral confinement can be approximated by $\sigma_T \approx \frac{\sigma_y \xi}{r_1}$, where σ_y is the yield stress of the sleeve material, ξ is the wall thickness of the sleeve, and r_1 is the inner radius of the sleeve. Moreover, the length of the sleeve is designed to be larger than the granite specimen; two maraging steel plugs with the same diameter as the granite specimen are applied to the confinement cell in order to axially load *only* the granite specimen. Thus, the signal measured from the transmitted bar can be used to calculate the stress in the granite sample. It is to be noted that the yield stress of the maraging steel plugs is expected to be in the range 1800 to 2400 MPa with a Rockwell hardness of HRC 55 to 58. Because of the high yield stress of the steel plugs, they are expected to remain in the elastic deformation regime during testing of the granite rocks under confinement.

[15] For unconfined experiments, the engineering stress, engineering strain rate and the engineering strain in the specimen are obtained by *Kolsky* [1949]

$$\sigma = E_b \frac{A_b}{A_s} \varepsilon_T(t); \quad \dot{\varepsilon} = -2\frac{c_b}{l_s}\varepsilon_R(t); \text{ and } \quad \varepsilon = \int_0^t \dot{\varepsilon}(t)dt \qquad (2)$$

In equation (2), E_b, A_b and C_b are Young's modulus, the cross-sectional area, and longitudinal wave speed of the steel bar, respectively; A_s and l_s are the cross-sectional area and the length of the granite specimen; and ε_T (t) and ε_R (t) are the transmitted and reflected engineering strain signals measured on the bars, respectively.

[16] For confined experiments, the engineering stress, engineering strain rate and engineering strain in the specimen are obtained as

$$\sigma = E_b \frac{A_b}{A_s} \varepsilon_T(t); \quad \dot{\varepsilon} = -\frac{2}{l_s}\left[c_b \varepsilon_R(t) + \dot{\sigma}(t)\frac{l_{plug}}{E_{plug}}\right]; \\ \text{and } \varepsilon = \int_0^t \dot{\varepsilon}(t)dt \qquad (3)$$

In equation (3), l_{plug} and E_{plug} are the length and Young's modulus of the steel plugs respectively. The true stress and true strain rate in the granite samples can be determined from the engineering stress and strain rate by assuming uniform and isochoric deformation conditions to prevail within the specimen during the deformation process. For brittle specimens the true stress versus true strain curves are expected to be quite similar to the engineering stress versus strain curves until large scale microcracking and failure set in after which the condition of isochoric deformation can be violated.

3. Experimental Results

3.1. Unconfined Experiments

[17] Table 1 is a summary of all the unconfined experiments conducted in the present study. The Westerly granite used in this study was even textured with a mean grain size of 0.7 mm. The samples used for testing were cylindrical disks with a diameter of ~10.2 mm and height varying from 6 to 8 mm. All granite specimens were cut with the same orientation from a single block of material. The plane of cut was not specifically orientated with respect to the foliation plane of the granite. The pulse duration and the pulse amplitude and strain rate in the samples were controlled by varying the striker bar length and the impact velocity, respectively. Posttest examination of the samples yield three

Table 1. Summary of All Unconfined Experiments Conducted on Westerly Granite

Shot	Specimen Height (mm)	Specimen Diameter (mm)	Striker Bar Velocity (m/s)	Striker Bar Length (inches)	Average Strain Rate (1/s)	Posttest Specimen
1	7.5	10.22	2.6	8	150	Fractured
2	7.21	10.22	3.2	8	120	Fractured
3	7.93	10.22	3.3	8	190	Intact/Fractured
4	7.21	10.21	4.4	8	245	Fractured/Pulverized
5	7.62	10.21	5.4	8	510	Pulverized
6	6.87	10.22	6.6	8	650	Pulverized
7	7.78	10.22	11.0	8	1300	Pulverized
8	6.36	10.22	3.8	4	180	Fractured
9	6.42	10.22	4.7	4	330	Pulverized
10	7.68	10.22	4.8	4	350	Pulverized

different final states: (1) Intact, or the nonfractured state, where insufficient loading (both stress amplitude and strain rates) did not lead to specimen fracture; (2) a fractured state, where the sample was split by a few longitudinal fractures–a common failure pattern observed during uniaxial loading at low strain rates; and (3) a pulverized state, where the sample is pervasively fractured, with fragment of size of less than 1 mm.

[18] Figure 3a shows the true stress versus true strain curves for all unconfined experiments conducted by using an 8 inch striker (pulse duration ~180 μs after pulse shaping). In the experiments the true strain rate in the samples varied from 200/s (shot 1) to 1500/s (shot 7). Figure 4a shows the true stress versus true strain curves for all the unconfined experiments conducted by using an 4 inch striker bar, in which the pulse duration was ~120 μs; the true strain rate varied from 200/s (shot 8) to 350/s (shot 10) in these experiments. Figures 3b and 4b show low magnification pictures of the corresponding posttest impacted specimens obtained using the 8 inch and 4 inch striker bars, respectively. From the results, it can be seen that the pulse duration has very little effect on the dynamic peak strength and failure of the granite samples. The impact velocity threshold for pulverization is about 4.5 m/s, which corresponds to a critical strain rate of ~300/s; specimens completely fail and become pulverized when the impact velocity is above 4.5 m/s (strain rates >300/s), while specimens remain intact or fail partially (discrete fractures) when the impact velocity is below 4.0 m/s (strain rates <200/s). In this way, the strain rate region in between 200/s and 300/s represents a transition zone between fracturing and pulverization for Westerly granite. In this region, the peak stress in the samples varies from 100 to 230 MPa with about 175 MPa required for failure; the strain to failure was about 0.75%. This transition is further confirmed by Shot 4, for which the peak stress in the sample was 210 MPa and the damage in the sample is best described by the label *fractured/pulverized*.

[19] To perform in situ recording of the deformation and failure processes, an Imacon 200 ultrahigh speed digital camera (DRS Technologies) is employed. In the video, 16 pictures are taken with interframe time of 20 μs in order to maximize imaging of the deformation and failure processes. Figure 5 shows the pulverization process for shot 7. The first frame corresponds to the time when the stress wave reaches the granite specimen. It is clearly seen that the specimen fails from the third frame onwards and eventually becomes completely pulverized.

[20] Transitions in dynamic failure mode in rock samples from discrete fracture to extensive fragmentation has also been previously investigated by *Li et al.* [2005] and *Zhou et al.* [2008] for rock mining applications, where they studied the relationship between specimen diameter and loading rate on the failure of unconfined rock samples. More importantly, they also showed that a critical strain rate was essential to induce fragmentation in rocks during the dynamic compressive loading below which the posttest specimens were essentially observed to be intact; moreover, they reported the critical strain rate levels to decrease as the specimen size became larger [*Li et al.*, 2008; *Lok et al.*, 2002].

3.2. Confined Experiments

[21] In this series of experiments three different sleeve materials are used to apply varying levels of confinement pressures on the granite specimens. The sleeve materials, their quasi-static yield strength, and maximum confinement pressure they can be used to apply, are listed in Table 2. In all the confined experiments granite specimens with length of 4 mm and diameter of 6 mm were employed. In all cases the length of the sleeve was 6 mm. The average wall thickness for the copper and brass sleeves was 1.5 mm, while the wall thickness for the PMMA sleeves was 1.1 mm. The steel plugs have a length of 3 mm and a diameter of 6 mm. The Westerly granite specimens used for the confined experiments were ground cylindrical to within 0.01 mm on the lateral surface with two end surfaces parallel to within 0.01 mm over the diameter of the specimen. The inner surfaces of sleeves were ground to the desired diameter, which has a predetermined misfit to the granite specimen. The misfit was designed to take the sleeve to yielding during shrinkage. The expected confinement pressures of 20 MPa (with PMMA), 60 MPa (with copper) and 132 MPa (with brass), correspond to depths of 1.1 km, 3.3 km and 7.3 km, respectively, assuming hydrostatic pore pressure. These estimates of depth are based on effective confining pressure, i.e., the solid pressure minus the pore fluid pressure. A good rule of thumb for confining pressure, assuming saturated rock densities and that water fluid pressure is hydrostatic (due to the weight of interconnected water from the surface to the depth of interest), is 18z, where z is the depth in km and the pressure is in MPa. However, during dynamic deformation, the pore fluid pressure is expected to be affected by both deformation as well as dilatancy. Under these conditions, it is not clear what the role of pore fluid pressure would be, since, as a result of dilatancy, the pore

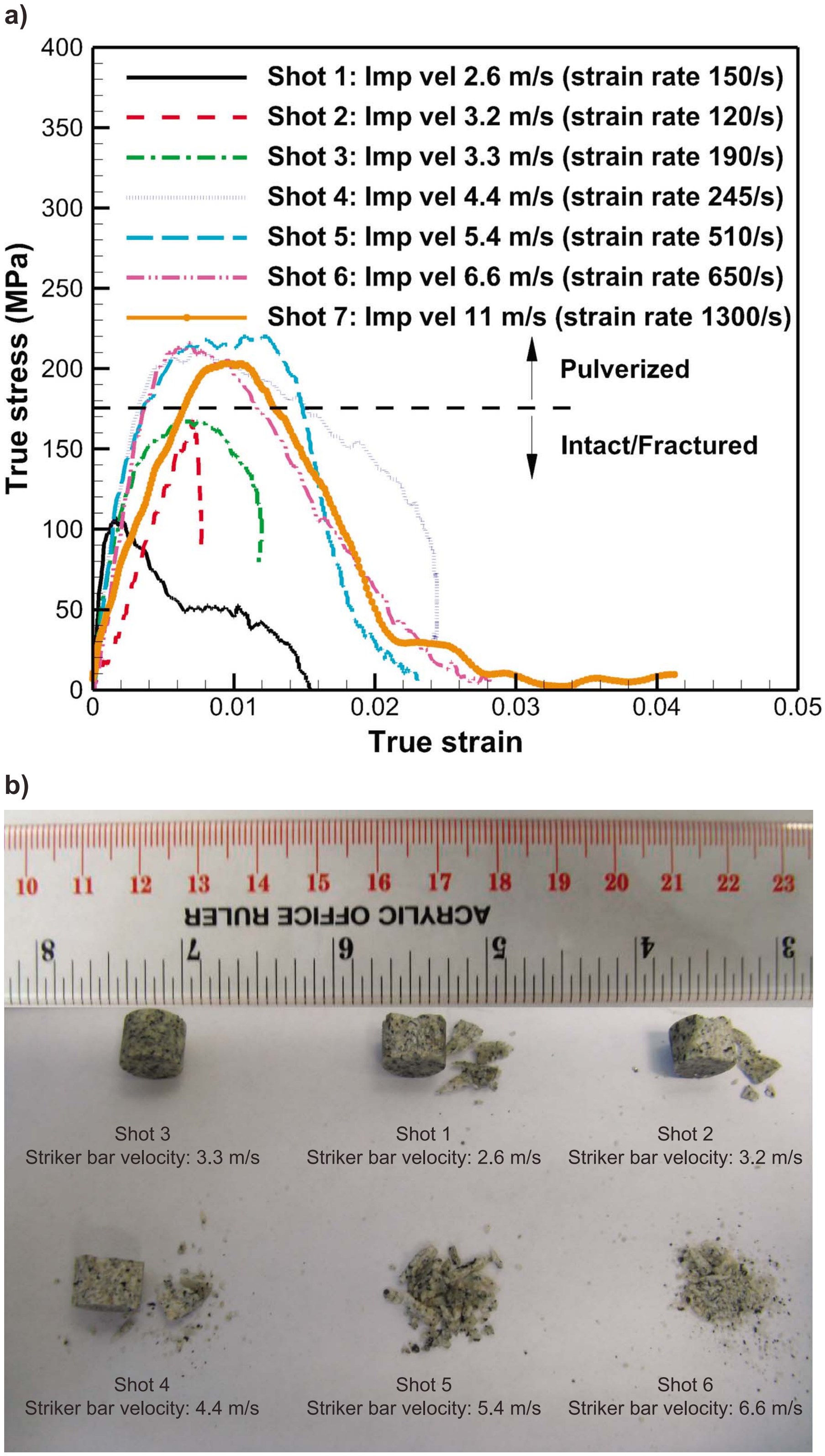

Figure 3. (a) Stress versus Strain curves for all the unconfined experiments conducted by using the 8 inch striker bar. (b) The corresponding posttest Westerly granite specimens showing the damage state for Shots 4, 5 and 6.

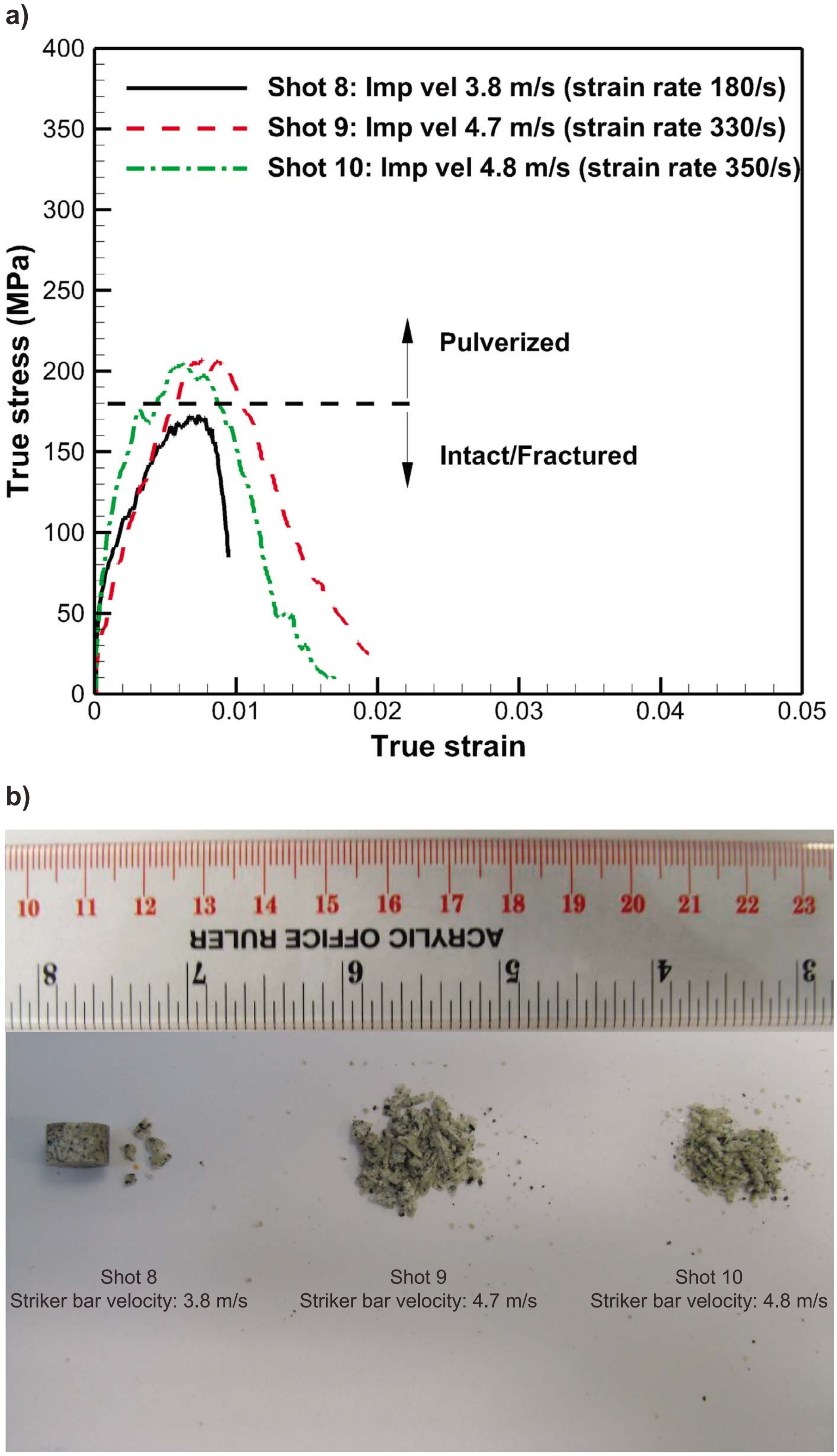

Figure 4. (a) Stress versus Strain curves for all the unconfined experiments conducted by using the 4 inch striker bar. (b) The corresponding posttest Westerly granite specimens showing the damage state for Shots 8, 9 and 10.

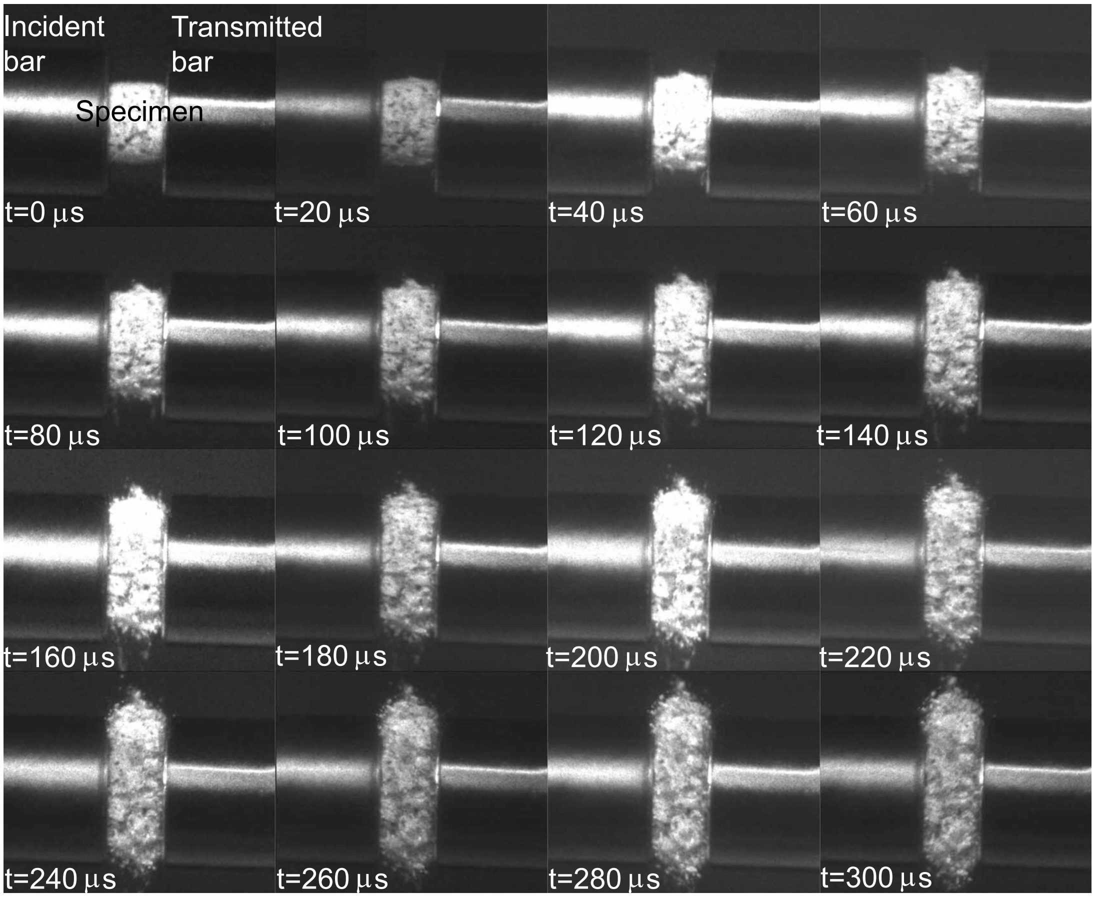

Figure 5. High-speed camera pictures for a typical unconfined experiment, Shot 7.

fluid pressure may drop down so much that these confinement pressures may correspond to perhaps shallower depths.

[22] Table 3 is a summary of all the experiments conducted in the present study with lateral confinement. Like in the case of the unconfined experiments, the posttest impacted specimens were divided into three damage states–intact, fragmented and pulverized.

[23] Figure 6a shows the true stress versus true strain curves obtained from the confined experiments with copper sleeve. As mentioned earlier, the estimated 60 MPa of confinement corresponds to a seismogenic depth of 3.3 km. Figure 6b shows low magnification pictures of the corresponding posttest specimens. The peak stress in the specimen increases from 210 MPa for the case of no confinement to about 850~1050 MPa at a confinement pressure of ~60 MPa. Moreover, the true stress in the specimen increases with strain up to ~2.6%, after which the stress in the specimen saturates at ~800 MPa. When the applied stress is lower than 800 MPa, in other words when the impact velocity is lower than 5.2 m/s (strain rate <460/s), the granite specimen remains intact with no apparent cracks on the impact faces. As seen in Figure 6b, a dominant single crack can be seen when the impact velocity is 10.0 m/s (strain rate ~970/s); multiple fractures can be seen when the impact velocity is increased to 13.1 m/s (strain rate ~1580/s), while the granite specimen becomes essentially a powder when the impact velocity is 15.1 m/s (strain rate ~1670/s).

[24] Figures 7a and 7b show the true stress versus true strain curves for confined experiments with PMMA and the brass sleeves, respectively. When the granite specimen is confined by PMMA sleeve (confinement pressure ~20 MPa), unlike the case of the experiments with the copper sleeve, a bell shaped true stress vs strain curve is observed. The peak stress in the specimens is ~450 MPa; the corresponding axial strain is 1.4%, after which the load carrying capacity of the granite specimens drops to nearly zero. As observed from Figure 7b, the behavior of the Westerly granite specimens when confined with the brass sleeves is very similar to those obtained with the copper sleeves except that the peak stress increases from 970 MPa to 1200 MPa at impact speeds of 10 m/s and higher. The post peak stress plateau levels are also higher–the stress is observed to saturate at a level of about 880 MPa and then remain essentially constant thereafter. However, unlike the tests conducted with confinement using PMMA and copper sleeves, for experiments conducted with the brass sleeves no pulverization of the granite specimens is seen even at strain rates as high as

Table 2. Sleeve Materials, Their Static Yield Stress, and the Corresponding Confinement Pressures

Sleeve Material	Yield Stress (MPa)	Confinement Pressure (MPa)
PMMA	55	20
Copper	120	60
SAE 72 brass	261	132

Table 3. Summary of All Experiments With Lateral Confinement

Shot	Specimen Height (mm)	Specimen Diameter (mm)	Striker Bar Velocity (m/s)	Average Strain Rate (1/s)	Confinement Pressure (MPa)	Posttest Specimens
P1	3.55	6.00	1.0	180	20	Intact
P2	4.21	6.00	3.5	290	20	Fractured/Pulverized
P3	4.00	6.00	3.5	340	20	Pulverized
P4	4.10	6.00	3.8	410	20	Pulverized
P5	4.25	6.00	4.4	460	20	Pulverized
P6	4.05	6.00	5.7	730	20	Pulverized
P7	4.25	6.00	10.8	1050	20	Pulverized
SC1	4.13	5.92	3.3	370	60	Intact
SC2	4.50	5.92	5.2	460	60	Intact
SC3	4.08	5.92	6.7	910	60	Fractured
SC4	4.07	5.92	7.6	1020	60	Fractured
SC5	4.20	5.92	10.0	970	60	Fractured
SC6	4.04	5.92	13.1	1580	60	Fractured/Pulverized
SC7	4.25	5.92	15.1	1670	60	Pulverized
B1	3.92	6.00	4.1	430	132	Intact
B2	4.28	6.00	7.1	620	132	Fractured
B3	4.01	6.00	8.5	710	132	Fractured
B4	4.15	6.00	9.8	1110	132	Fractured
B5	4.16	6.00	12.7	1500	132	Fractured
B6	4.48	6.00	16.3	1860	132	Fractured

1860/s. Also, below an impact velocity of 7 m/s the granite specimen remains essentially intact with no apparent cracks on the impact faces.

[25] When the granite specimen fails, the peak stress levels (in Figures 3a, 6a, 7a, and 7b) can be defined as the dynamic compressive strength of the Westerly granite under a given level of lateral confinement. Figure 8 shows the dynamic compressive strength versus the lateral confinement pressure for all the confined experiments. The dynamic compressive strength of the granite increases from 210 MPa to approximately 1200 MPa as the lateral confinement pressures are increased from zero (unconfined) to 132 MPa (confinement with brass sleeve). Recall that experiments with the brass sleeve confinement show only dynamic fracture of the specimens into large fragments but no pulverization at the strain rates employed in the present investigation. This suggests that pulverization may be found in the shallow subsurface (as also confirmed by borehole studies) and at burial depths of ~3.3 km. Currently, plate impact shock compression studies on Westerly granite are underway in our laboratory (where both confining pressures as well as the strain rates are much higher than those discussed here), and the results of these studies will be presented in a forthcoming paper.

[26] Figure 9 shows estimates of the threshold strain rate for the transition from fracture to pulverization in the Westerly granite specimens. Since the SHPB experiments were of the "recovery" type, in all cases fracture is assumed to occur during the first loading pulse. The solid right triangles show data for the case of no confinement. The average strain rate at which transition from fracture to pulverization is observed in the Westerly granite specimens is shown by the vertical dashed line at a strain rate of ~250/s. The solid squares and the solid circles represent data with PMMA and copper confinement sleeves with corresponding lateral confinement pressures of 20 MPa and 60 MPa, respectively. It is to be noted that in the presence of the higher confinement pressures both the peak stress as well as the critical average strain rates for transition are increased with the transition to pulverization occurring at 300/s and 1500/s, respectively. This increase in the strength, and hence the strain rate under confinement, has also been observed for other brittle materials under similar dynamic loading conditions [*Chen and Ravichandran*, 1997; *Huang et al.*, 2002; *Lankford*, 2004; *Subhash and Ravichandran*, 2000]. For the case of the brass sleeves, no threshold strain rate for pulverization can be identified from our experiments (note that the brass sleeves correspond to a confinement pressure of ~132 MPa, which corresponds to a buried depth of about 5 km). At these depths, the transition to pulverization will perhaps require much higher strain rates than those obtained in the current SHPB experiments.

[27] There are several indications in the field that show pulverization to occur at relatively shallow depths. First, the Punchbowl fault only 5 km southwest from the outcrops of pulverized rock bodies near the SAF is interpreted to have been exhumed from about 2 to 4 km [*Chester et al.*, 2004, and references therein]. Additional direct evidence of pulverization occurring at shallow depths is provided by studies [*Reches and Dewers*, 2005; *Wilson et al.*, 2005] of pulverized quartzite in fresh rupture zones in South African gold mines. They analyzed rock powder samples collected from the rupture zone of M = 3.7 earthquake at depth of about 2 km (and near large internal free surfaces), and found that the grain size distribution and other properties of those samples is similar to those found in Tejon Pass. Pulverized quartzites are also abundant in many fresh rupture zones in the mines [*Reches and Dewers*, 2005], forming under minimal or even negligible confining stress.

3.3. Scanning Electron Microscopy: Characterization of Damage and Fragmentation

[28] In order to understand the modes of damage as well as the degree of fragmentation in the posttest Westerly granite specimens, cross section of specimens confined by a copper sleeve were obtained by sectioning them parallel to the loading axis using a low speed diamond saw. The SEM images of these sections were then compared to those

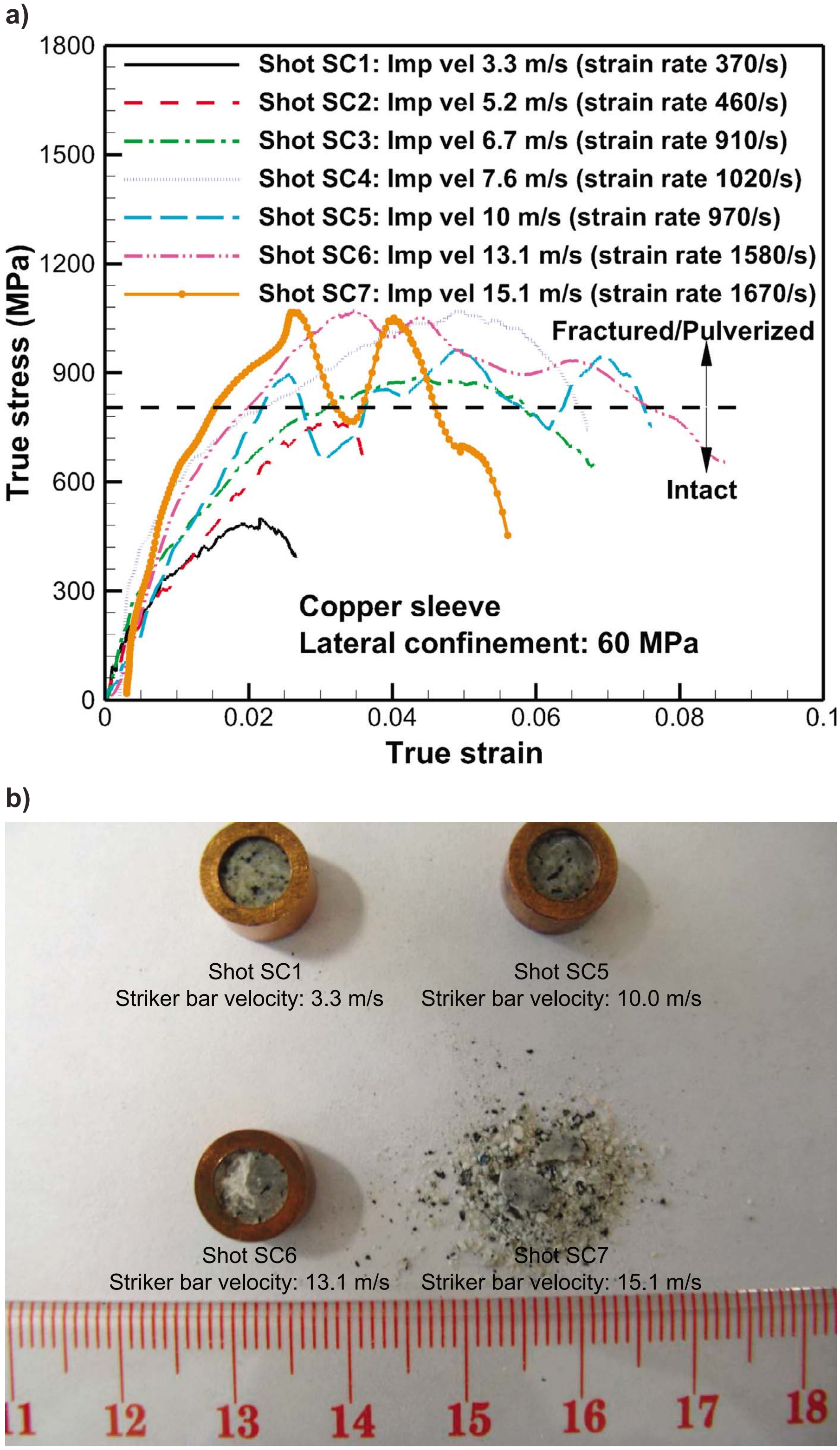

Figure 6. (a) Stress versus Strain curves for the confined experiments with copper sleeve. (b) The corresponding posttest Westerly granite specimens showing the damage state for Shots SC1, SC5, SC6 and SC7.

obtained from an untested specimen. Figure 10 shows a scanning electron microscopy map of a cross section taken from an untested specimen, while Figure 11 shows the SEM map for a posttest impacted specimen, Shot SC4, that was impacted with a velocity of 7.6 m/s. Compared with untested specimen, the posttest recovered specimen, SC4, shows a few localized damaged areas with multiple fractured grains indicating localized pulverization, even though

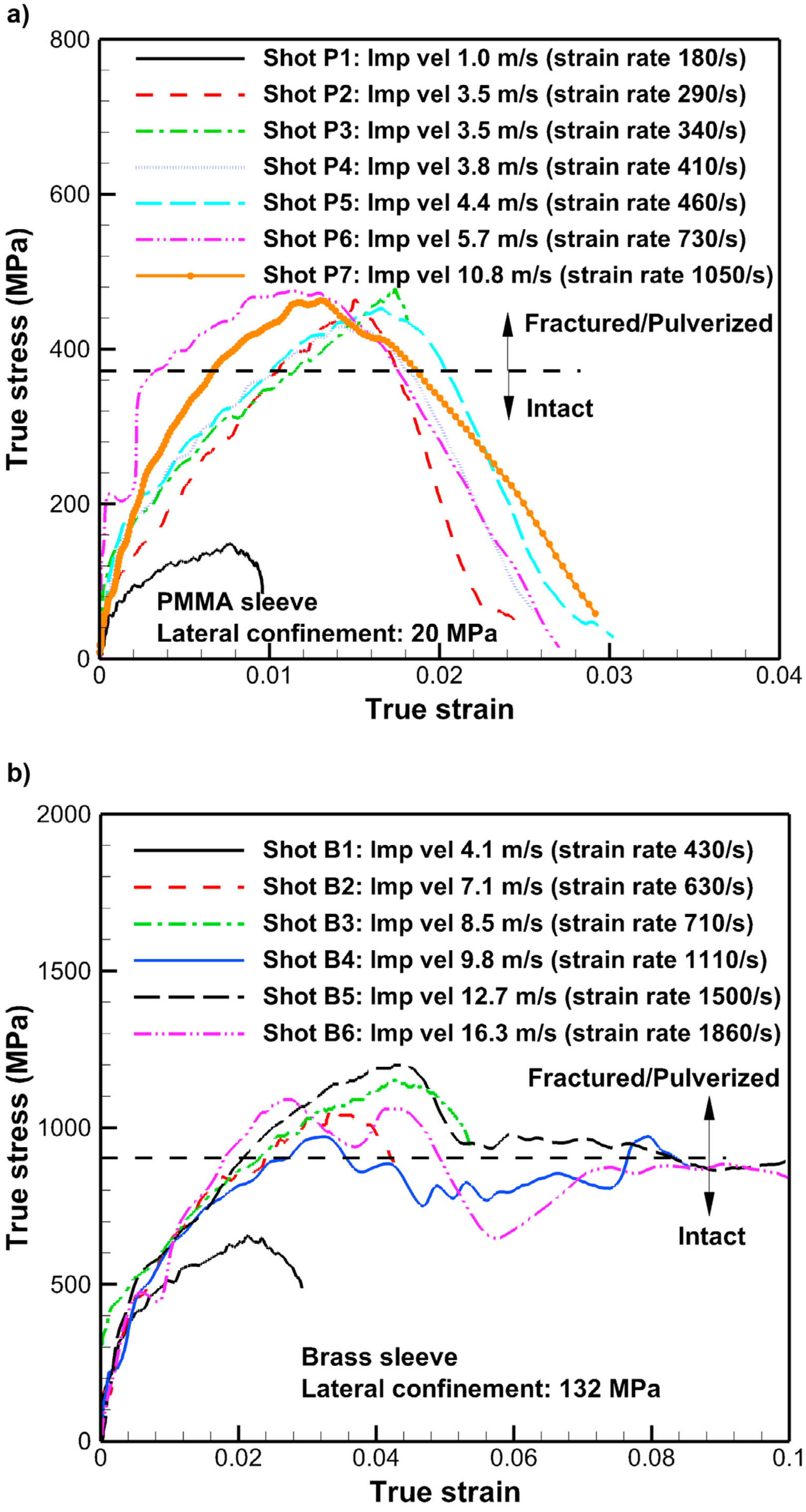

Figure 7. (a) Stress versus Strain curves for the confined experiments with PMMA sleeve. (b) Stress versus Strain curves for the confined experiments with brass sleeve.

there was no apparent visible fracture at the impact surface. These highly deformed regions are understood to form as a result of systematic intergrain contact and sliding, intragrain fracturing, and void collapse, which are promoted by the amplification of the grain-to-grain contact stresses, and facilitated by the formation of the stress chains. Figure 12 shows the scanning electron microscopy map of the cross section surface parallel to the loading axis for shot SC5, conducted at an impact velocity of 10.0 m/s. At this higher impact velocity, the specimen shows extensive micro-

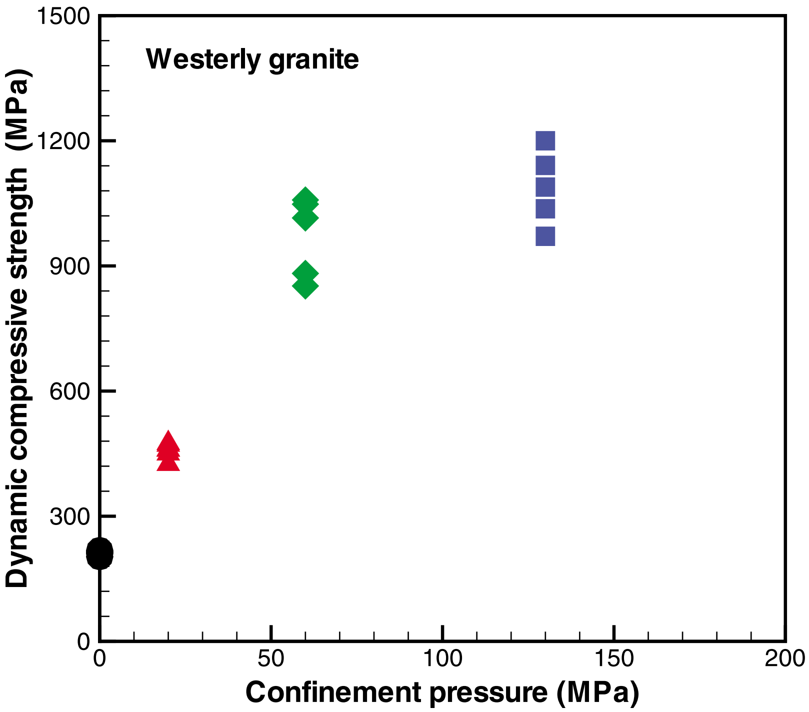

Figure 8. Dynamic compressive strength versus the lateral confinement pressure for all the confined experiments conducted in the present study using copper, PMMA and brass sleeves.

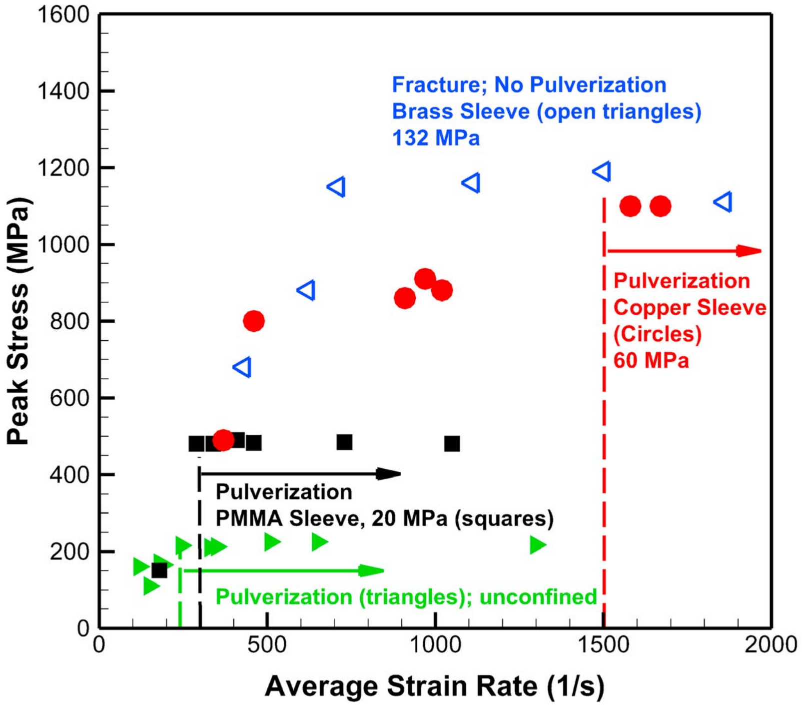

Figure 9. Peak stress as a function of the average strain rate in Westerly granite specimens for the case of no confinement, and confinement with PMMA, copper and brass sleeves. The threshold for transition from sparse fracture to pervasive pulverization increases as the confinement stress is increased. For the case of the brass sleeve, no critical transition strain rate could be identified from the present experiments.

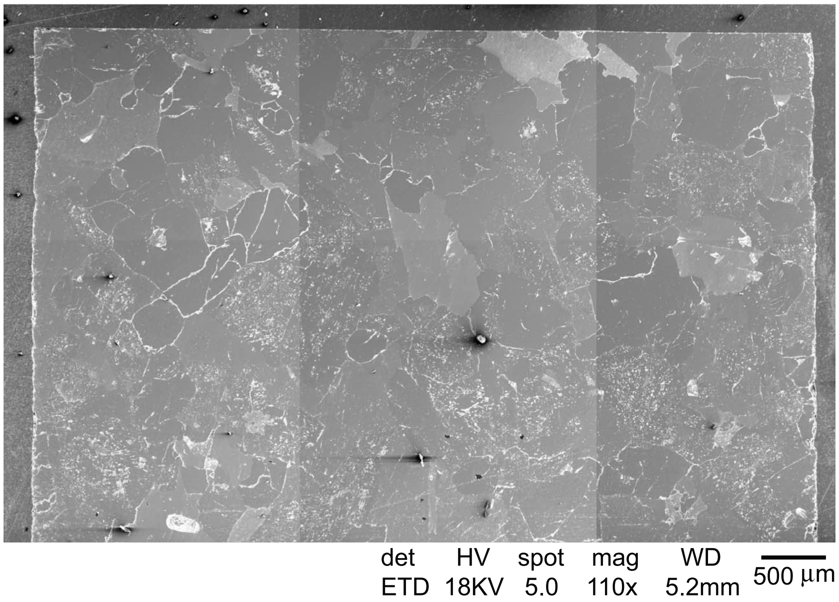

Figure 10. SEM image of a section perpendicular to the loading axis of an untested Westerly granite specimen.

cracking throughout the specimen as well as a larger localized pulverized region when compared to the impact velocity of 7.6 m/s. Figure 13 shows the scanning electron microscopy image of the cross section surface parallel to the loading axis for shot SC6, conducted an impact velocity of 13.1 m/s. At this higher impact velocity, the specimen shows several cracks along with regions of pervasive pulverization. In the lower half of the specimen, there are regions that show extensive pulverization and that have been reduced to essentially a powder and fell out of the sample sleeve so this region could not be sectioned. Also, most particles in the pulverized regions have dimensions of 500 microns or less. These particle size dimensions are consistently higher than those recovered from the field, which have been reported to be 300 microns or less. However, it must be noted that these submillimeter-scale particles have formed under a single impact loading under uniaxial stress conditions. The natural state in the field are

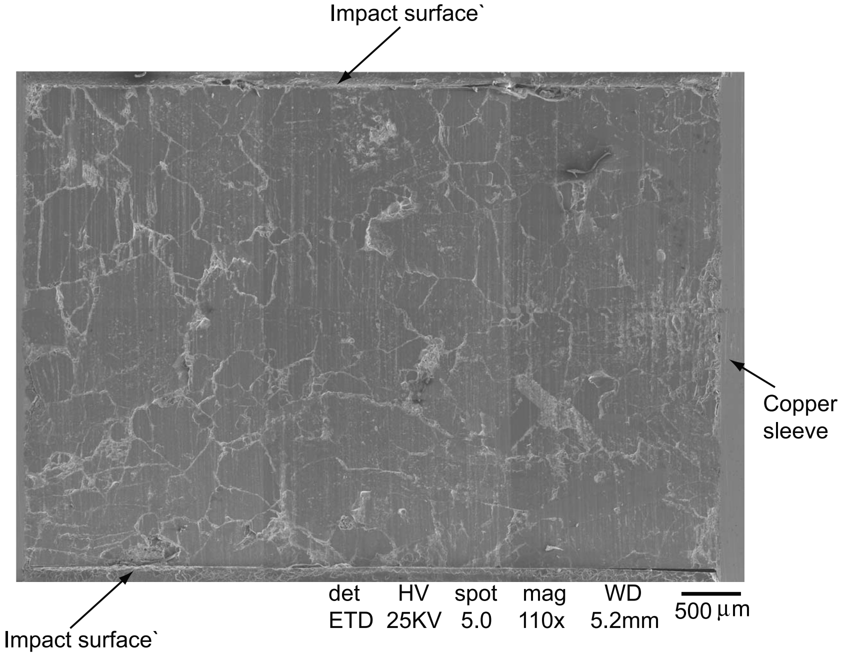

Figure 11. SEM image of a section perpendicular to the loading axis of a posttest recovered specimen from Shot SC4 (impact velocity 7.6 m/s) confined with a copper sleeve.

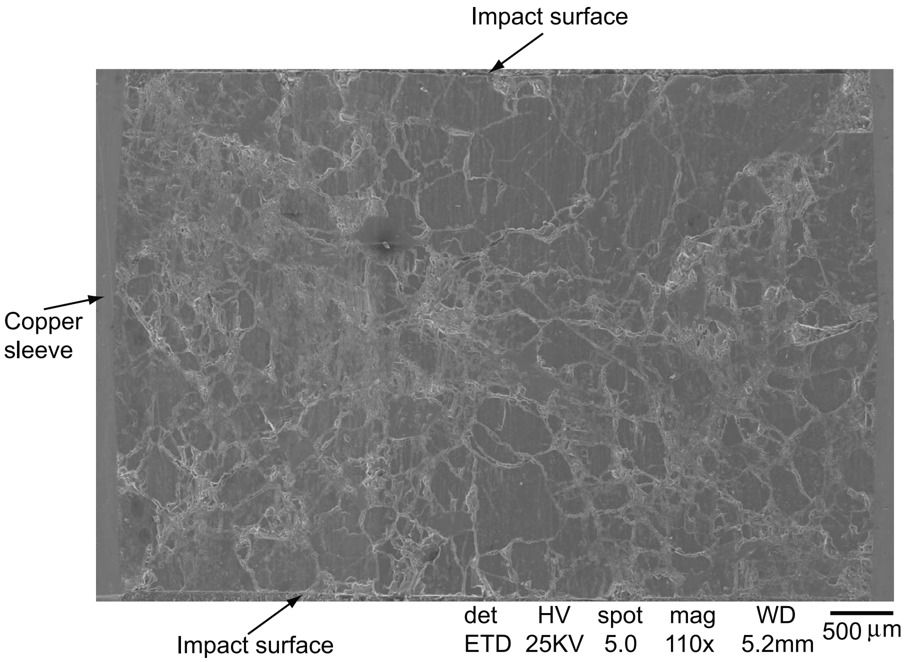

Figure 12. SEM image of a section perpendicular to the loading axis of a posttest recovered specimen from Shot SC5 (impact velocity 10.0 m/s) confined with a copper sleeve.

perhaps a result of several earthquakes, each one damaging the rocks by compression and shear loadings.

4. Possible Mechanisms for Rock Fracture and the Origin of Pulverization Rocks Along Natural Faults

[29] In an attempt to understand the origin of PR in the field, we turn our attention to the few early theoretical studies on dynamic shear rupture. *Freund* [1990] obtained a steady state asymptotic solution for the stress and particle velocity fields near a Mode II shear crack propagating at sub-Rayleigh and intersonic speeds along a prescribed straight line path in a homogeneous, isotropic, linear elastic material. According to this solution, when the crack tip speed v, is sub-Rayleigh ($0 < v < c_R$) the asymptotic stress fields are square root singular, and the dominant term in the near tip stress components, σ_{ij}, viewed from a local coordinate system propagating with the crack tip at speed take the form

$$\sigma_{ij}(\eta_1, \eta_2) = K_{II}^d(t)\frac{f_{ij}(\theta_l, \alpha_l, \alpha_s)}{r_l^{1/2}} \qquad (4)$$

where (η_1, η_2) are the coordinates of a point with respect to the mathematical crack tip, i.e., moving Cartesian coordinate system attached to the crack tip (with the η_1 axis perpendicular to the crack edge and η_2 axis perpendicular to the

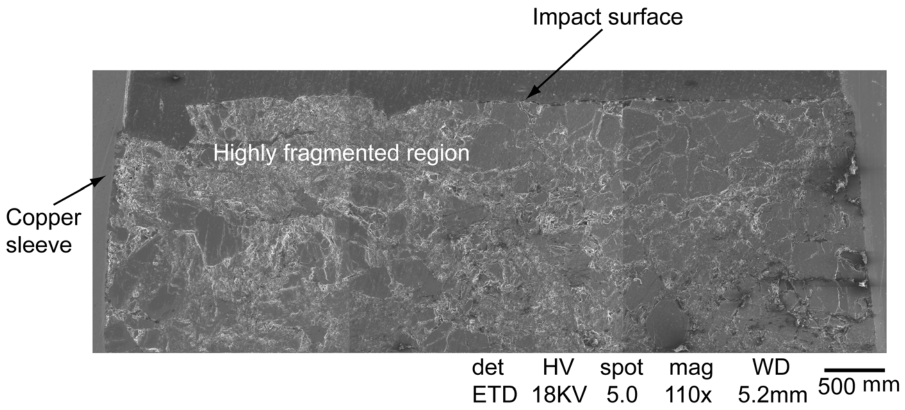

Figure 13. SEM image of a section perpendicular to the loading axis of a posttest recovered specimen from Shot SC6 (impact velocity 10 m/s) confined with a copper sleeve showing the highly fragmented region from the upper half of the recovered specimen. The lower half of the specimen was pulverized to essentially a powder.

plane of the crack), f_{ij} (.,.) are known functions of crack tip speed and angular position, the indices ij have the range of 1, 2, 3, while the variables r_l, θ_l, α_l, and α_s are defined as follows:

$$r_l = \sqrt{\eta_1^2 + \alpha_l^2 \eta_2^2}; \quad \theta_l = \tan^{-1} \frac{\alpha_l \eta_2}{\eta_1} \tag{5}$$

$$\alpha_l = \sqrt{1 - \frac{v^2}{c_l^2}}; \ \alpha_s = \sqrt{1 - \frac{v^2}{c_s^2}} \tag{6}$$

As it is evident from the general form of this solution, the six independent components of the stress tensor all share a common amplitude factor K_{II}^d, which in turn is called the mode II dynamic stress intensity factor.

[30] Based on the crack tip fields, as described by equations (4) to (6), for sub-Rayleigh rupture speeds the deformation conditions at material points a few mm away from the rupture tip are extreme: tensile stresses approach 5 GPa, volumetric strain rates exceed 10^5 s^{-1}, and volumetric expansion alternates with volumetric contraction [*Reches and Dewers*, 2005]. Under these conditions, it is expected that a localized zone (a few mm wide) will be pulverized all along the rupture path. Similar, PR formations are also expected to form during dynamic slip along a somewhat rough fault with amplitude to wavelength ratio of the surface roughness on the order of 0.001 to 0.01, as argued by *Walter and Brune* [1993], *Chester and Chester* [2000], and *Power and Tullis* [1989, 1995]. However, these mechanisms cannot explain the origin of PR observed in the field, which has been observed, in some cases, to extend almost 100 m away from the fault plane.

[31] In the case of homogeneous fault interfaces, sub-Rayleigh shear ruptures have been shown to produce damage zones consisting of an array of tensile cracks [*Griffith et al.*, 2009]. These cracks nucleate and grow over the length of the cohesive zone behind the tip of the shear rupture front that propagates dynamically along the fault interface. The tensile cracks are produced only along one side of the interface where transient, fault-parallel, tensile stress perturbations are associated with the growing shear rupture tip. The possible relation of these cracks to geological observations of periodic arrays of tensile, off-fault, fractures and to pseudotachylyte injection veins has been hypothesized by *Rosakis* [2002]. Also, *Di Toro et al.* [2005a, 2005b] have provided field evidence that tensile fractures containing pseudotachylyte (pseudotachylyte injection veins) might indeed form by a similar dynamic process. However, again this damage is expected to be limited to tensile cracks in a thin region (tens of mm) off the rupture fault, and is unlikely to explain the origin of PR observed in the field tens of meters away from the fault plane.

[32] Moreover, in the case of sub Rayleigh rupture propagation along nonhomogeneous fault interfaces, theory [*Ben-Zion*, 2001] shows that mode II ruptures on a material interface tend to evolve wrinkle-like pulses that propagate preferentially in the direction of motion of the slower velocity block. The theory [*Ben-Zion and Shi*, 2005] also shows that more damage is expected on the side of the fault with higher seismic velocity, which for the preferred propagation direction is the side that is consistently in the tensional quadrant of the radiated seismic field. This asymmetry in damage pattern is consistent with the overall distribution of pulverized rocks along the SAF in the Mojave, and with other smaller scale observations of damage distribution across the SAF in this area [*Dor et al.*, 2006a]. Seismic imaging [*Fuis et al.*, 2003] suggests that the northeast more damaged side of the SAF in the Mojave has faster seismic velocities. This correlation is compatible with northwestward preferred direction of large ruptures along the SAF in the Mojave. However, if the Weertman pulse were to induce pulverization, we would expect to find pulverized rocks along faults separating the bimaterial fault interface, with no evidence for compression. However, pulverized sandstone along the San Andreas fault is understood to show compression features [*Dor et al.*, 2009]. Also, PRs are sometimes found on both sides of the San Andreas fault.

[33] The results of the SHPB experiments described herein clearly show that for granite under dynamic compression, a minimum threshold strain rate of 250/s is required for transition from sparse fracturing to pervasive pulverization, below which the transition to pulverization is highly unlikely. Even though equations (4) to (6) predict high strain rates for material points in or near the fault core, at distances away from the fault core (tens of meters) the *effective* strain rates, $\dot{\bar{\varepsilon}} = \frac{1}{1+\upsilon}\sqrt{\frac{3}{2}\dot{\varepsilon}_{ij}^{dev}\dot{\varepsilon}_{ij}^{dev}}$, where $\dot{\varepsilon}_{ij}^{dev} = \dot{\varepsilon}_{ij} - \frac{1}{3}tr(\dot{\varepsilon})\delta_{ij}$, at 1–2% effective strains are expected to be several orders of magnitude smaller (~1/s), and, in view of the present experimental results, are not likely to result in pulverization. Hence we propose that an alternative mechanism, supershear rupture, that can generate very high effective strain rates at distances far away from the rupture plane that may lead to pulverization of rocks.

[34] For the case of the mode II shear rupture propagating at intersonic speeds along a straight line, the dominant term governing the stress state near the rupture tip is of the form [*Samudrala et al.*, 2002],

$$\sigma_{ij}(\eta_1, \eta_2) = K_{II}^*(t)\left\{\frac{f_{ij}(\theta_l, \alpha_l, \hat{\alpha}_s)}{r_l^q} + \frac{g_{ij}(\alpha_l, \hat{\alpha}_s)}{(-\eta_1 - \hat{\alpha}_s|\eta_2|)^q}H(-\eta_1 - \hat{\alpha}_s|\eta_2|)\right\} \tag{7}$$

where g_{ij} (·) is a function of the crack tip speed, H (·) is the Heaviside step function, q is the singularity exponent given by

$$q = \frac{1}{\pi}\tan^{-1}\frac{4\alpha_l\hat{\alpha}_s}{\left(1 - \hat{\alpha}_s^2\right)^2} \tag{8}$$

$$\hat{\alpha}_s = \sqrt{\frac{v^2}{c_s^2} - 1} \tag{9}$$

K_{II}* (t) is the intersonic stress intensity factor defined as

$$K_{II}^*(t) = \lim_{r_l \to \infty} \sqrt{2\pi}\, r_l^q\ \sigma_{12}(r_l, 0) \tag{10}$$

From equation (7) we see that the asymptotic solution predicts two traveling waves of strong stress discontinuity attached to the crack tip and inclined at $\beta = \tan^{-1}(1/\hat{\alpha}_s) = \sin^{-1}(c_s/v)$ to the crack faces. The stress field is singular at the crack tip, and the singularity exponent q is a function of the crack tip speed. Exponent q increases monotonically from 0 at $v = c_s$ to a value of 1/2 at $v = \sqrt{2}c_s$, and there after decreases monotonically to 0 at $v = c_l$. The stresses are also singular all along the lines of discontinuity with the same strength of singularity as that at the rupture tip. The crack tip singularity is thus radiated away from the tip to create two *shear shock waves*. As one would expect, the existence of infinite stress jumps across these shock waves is not feasible and such a prediction is an artifact of the theory of linear elasticity. In real materials, however, this prediction corresponds very well with well-defined lines across which large but finite stress jumps occur. The pathology of infinite stress jumps and zero crack tip energy release rate for an intersonic mode II crack can be overcome by introducing a process zone of finite size ahead of the tip. Such a solution is given by *Samudrala et al.* [2002]. The cohesive zone solution also introduces some structure across the shock wave by smearing out the stress jump and eliminating the singularities.

[35] With regards to the origin of PR, the point to note is that supershear ruptures induce a shock wave. Simple models, such as those described by equations (7) to (10) provided by *Samudrala et al.* [2002], yield Heaviside functions that permit sharp fronts and with small decay with distance. In this way, very high effective strain rates can be achieved at relatively small effective strains tens of meters from the fault core, as supershear rupture induces a shock wave and generates high frequency displacements. This is consistent with the discovery of pulverized rocks only near large strike-slip faults: San Andreas and San Jacinto faults in California [*Dor et al.*, 2006b, 2009] and Northern Anatolia fault in Turkey [*Bouchon and Rosakis*, 2002], both of which are amenable to supershear rupture.

[36] It is to be noted that intersonic ruptures lead to the formation of shear Mach cones at material points away from the fault plane. This state of stress is quite different from axial compressive loading and lateral confinement used in the present experiments to understand the transition of damage from sparse fracture to pervasive pulverization in Westerly granite. To the best of the authors' knowledge no systematic studies are available in the literature that provide insights into such transitions with strain rate in rocks under dynamic shear loading. In view of these limitations, we have used results of the SHPB experiments and the associated strain rates to better understand the conditions that can possibly constrain the origin of pulverized rocks as observed in the field. Of course, insufficient experimental data exist to demonstrate whether the effective strain rate approach is valid for Westerly granite, except for under uniaxial compression and perhaps tension. It is, nevertheless, a useful approach and employs assumptions that are similar to those customarily engaged to predict strain rate-sensitive behavior including failure in engineering brittle materials under dynamic multiaxial loading conditions [*Meyers*, 1994].

5. Summary

[37] In the present study, split Hopkinson pressure bar (SHPB) recovery experiments are conducted on Westerly granite samples under both unconfined and confined loading conditions to investigate the threshold for transition in deformation mode from sparse fracture to pervasive pulverization under stress wave loading conditions. Well-characterized lateral confinement is generated in the cylindrical specimens by utilizing shrink fit PMMA and metal sleeves around the specimens during dynamic loading. The unconfined condition represents the natural rocks on the surface ground, while the different lateral confined conditions represent different buried depth of natural rocks.

[38] The results of the study indicate that for transition from sparse fracture to pervasive pulverization in rocks (Westerly granite), high strain rate loading conditions (effective strain rates in excess of 300/s) are necessary and that the formation of PR may be inhibited at larger depths under higher confinement pressures. As seen in Figures 6 and 7, the strain corresponding to the peak stress in the Westerly granite samples varies from 0.8% for the case of no confinement to about 1.5% in the case of the PMMA sleeves (20 MPa confinement) to about 3.6% for the case of the copper sleeve confinement (60 MPa). These relatively small levels of strain are consistent with the basic fabric structure of the pulverized rocks recovered in the field.

[39] The constraints of relatively low strains (1–3%) observed in PR recovered from the field and the existence of a threshold strain rate of ~250/s and higher for pulverization of rocks, combined with field observations that PR has been found in belts that stretch tens of meters away from the rupture fault plane, indicate that a dynamic supershear-type rupture may be necessary for the origin of pulverized rocks observed in both large strike-slip-type earthquakes and also the relatively small slip dip-slip-type of fault ruptures observed in nature.

[40] **Acknowledgments.** The authors would like to acknowledge the National Science Foundation Earth Division (EAR:0710975 and EAR:0810083) for providing financial support for conducting the present research. The authors from CWRU would also like to acknowledge the National Science Foundation for the Major Research Instrumentation awards MRI CMMI 0079458 and MRI CMMI 0521364 that were used to acquire the ultra-high-speed digital camera (DRS Hadland 200) and the SEM (FEI FE NanoSEM600) that were used to conduct the experiments reported in the manuscript.

References

Ashby, M. F., and C. G. Sammis (1990), The damage mechanics of brittle solids in compression, *Pure Appl. Geophys.*, *133*(3), 489–521, doi:10.1007/BF00878002.

Ben-Zion, Y. (2001), Dynamic ruptures in recent models of earthquake faults, *J. Mech. Phys. Solids*, *49*, 2209–2244, doi:10.1016/S0022-5096(01)00036-9.

Ben-Zion, Y., and Z. Q. Shi (2005), Dynamic rupture on a material interface with spontaneous generation of plastic strain in the bulk, *Earth Planet. Sci. Lett.*, *236*(1–2), 486–496, doi:10.1016/j.epsl.2005.03.025.

Bouchon, M., and A. J. Rosakis (2002), Reply to comment on "How fast is rupture during an earthquake? New insights from the 1999 Turkey earthquakes," *Geophys. Res. Lett.*, *29*(8), 1243, doi:10.1029/2002GL015096.

Brune, J. (2001), Fault-normal dynamic loading and unloading: An explanation for "nongouge" rock powder and lack of fault-parallel shear bands along the San Andreas Fault, *Eos Trans. AGU*, *82*(47), Fall Meet. Suppl., Abstract S22B-0655.

Brune, J. N., S. Brown, and P. A. Johnson (1993), Rupture mechanism and interface separation in foam rubber models of earthquakes: A possible solution to the heat flow paradox and the paradox of large overthrusts, *Tectonophysics*, *218*, 59–67, doi:10.1016/0040-1951(93)90259-M.

Chen, W., and G. Ravichandran (1997), Dynamic compressive failure of a glass ceramic under lateral confinement, *J. Mech. Phys. Solids*, *45*, 1303–1328, doi:10.1016/S0022-5096(97)00006-9.

Chester, F. M., and J. S. Chester (2000), Stress and deformation along wavy frictional faults, *J. Geophys. Res.*, *105*(B10), 23,421–23,430, doi:10.1029/2000JB900241.

Chester, F. M., J. S. Chester, D. L. Kirschner, S. E. Schulz, and J. P. Evans (2004), Structure of large-displacement strike-slip fault zones in the brittle continental crust, in *Rheology and Deformation in the Lithosphere at Continental Margins*, edited by G. D. Karner et al., pp. 223–260, Columbia Univ. Press, New York.

Davies, E. D. H., and S. C. Hunter (1963), The dynamic compression testing of solids by the method of the split Hopkinson pressure bar, *J. Mech. Phys. Solids*, *11*, 155–179, doi:10.1016/0022-5096(63)90050-4.

Di Toro, G., G. Pennacchioni, and G. Teza (2005a), Can pseudotachylytes be used to infer earthquake source parameters? An example of limitations in the study of exhumed faults, *Tectonophysics*, *402*, 3–20, doi:10.1016/j.tecto.2004.10.014.

Di Toro, G., S. Nielsen, and G. Pennacchioni (2005b), Earthquake rupture dynamics frozen in exhumed ancient faults, *Nature*, *436*, 1009–1012, doi:10.1038/nature03910.

Doan, M.-L., and G. Gary (2008), Rocks pulverized near San Andreas Fault: Insight from high strain rate testing experiments, *Eos Trans. AGU*, *89*(53), Fall Meet. Suppl., Abstract S34B–06.

Doan, M.-L., and G. Gary (2009), Rock pulverization at high strain rate near the San Andreas Fault, *Nat. Geosci.*, *2*, 709–712, doi:10.1038/ngeo640.

Dor, O. (2006), Field guide for pulverized rocks along the Mojave section of the San Andreas Fault Zone, paper presented at Annual Meeting, South. Calif. Earthquake Cent., Palm Springs, Calif.

Dor, O. (2007), Symmetry properties, pulverized rocks and damage architecture as signatures of earthquake ruptures, Ph.D. thesis, Univ. of South. Calif., Los Angeles.

Dor, O., T. K. Rockwell, and Y. Ben-Zion (2006a), Geological observations of damage asymmetry in the structure of the San Jacinto, San Andreas and Punchbowl faults in Southern California: A possible indicator for preferred rupture propagation direction, *Pure Appl. Geophys.*, *163*(2–3), 301–349, doi:10.1007/s00024-005-0023-9.

Dor, O., Y. Ben-Zion, T. K. Rockwell, and J. N. Brune (2006b), Pulverized rocks in the Mojave section of the San Andreas Fault Zone, *Earth Planet. Sci. Lett.*, *245*, 642–654, doi:10.1016/j.epsl.2006.1003.1034.

Dor, O., Y. Ben-Zion, T. K. Rockwell, and J. N. Brune (2006c), Pulverized sedimentary rocks in the Mojave section of the San Andreas Fault Zone, paper presented at Annual Meeting, South. Calif. Earthquake Cent., Palm Springs, Calif.

Dor, O., J. S. Chester, Y. Ben-Zion, J. N. Brune, and T. K. Rockwell (2009), Characterization of damage in sandstones along the Mojave section of the San Andreas Fault: Implications for the shallow extent of damage generation, *Pure Appl. Geophys.*, *166*(10–11), 1747–1773, doi:10.1007/s00024-009-0516-z.

Freund, L. B. (1990), *Dynamic Fracture Mechanics*, Cambridge Univ. Press, Cambridge, U. K., doi:10.1017/CBO9780511546761.

Frew, D., M. Forrestal, and W. Chen (2002), Pulse shaping techniques for testing brittle materials with a split Hopkinson pressure bar, *Exp. Mech.*, *42*(1), 93–106, doi:10.1007/BF02411056.

Fuis, G. S., et al. (2003), Fault systems of the 1971 San Fernando and 1994 Northridge earthquakes, southern California: Relocated aftershocks and seismic images from LARSE II, *Geology*, *31*(2), 171–173, doi:10.1130/0091-7613(2003)031<0171:FSOTSF>2.0.CO;2.

Grady, D. E., and M. E. Kipp (1993), Dynamic fracture and fragmentation, in *High-Pressure Shock Compression of Solids*, edited by J. R. Asay and M. Shahinpoor, pp. 265–322, Springer, New York.

Griffith, W. A., A. Rosakis, D. D. Pollard, and C. W. Ko (2009), Dynamic rupture experiments elucidate tensile crack development during propagating earthquake ruptures, *Geology*, *37*(9), 795–798, doi:10.1130/G30064A.1.

Hadley, K. (1976), Comparison of calculated and observed crack densities and seismic velocities in Westerly granite, *J. Geophys. Res.*, *81*(20), 3484–3494, doi:10.1029/JB081i020p03484.

Huang, C. Y., G. Subhash, and S. J. Vitton (2002), A dynamic damage growth model for uniaxial compressive response of rock aggregates, *Mech. Mater.*, *34*(5), 267–277, doi:10.1016/S0167-6636(02)00112-6.

Kolsky, H. (1949), An investigation of the mechanical properties of materials at very high rates of loading, *Proc. Phys. Soc. B*, *62*(11), 676–700, doi:10.1088/0370-1301/62/11/302.

Lankford, J. (2004), The role of dynamic material properties in the performance of ceramic armor, *Int. J. Appl. Ceram. Technol.*, *1*(3), 205–210, doi:10.1111/j.1744-7402.2004.tb00171.x.

Li, X. B., T. S. Lok, and J. Zhao (2005), Dynamic characteristics of granite subjected to intermediate loading rate, *Rock Mech. Rock Eng.*, *38*(1), 21–39, doi:10.1007/s00603-004-0030-7.

Li, X.-B., L. Hong, T.-b. Yin, Z. Zi-long, and Z.-y. Ye (2008), Relationship between diameter of split Hopkinson pressure bar and minimum loading rate under rock failure, *J. Cent. South Univ. Technol.*, *15*, 218–223, doi:10.1007/s11771-008-0042-7.

Lockner, D. A. (1998), A generalized law for brittle deformation of Westerly granite, *J. Geophys. Res.*, *103*(B3), 5107–5123, doi:10.1029/97JB03211.

Lok, T. S., X. B. Li, D. Liu, and P. J. Zhao (2002), Testing and response of large diameter brittle materials subjected to high strain rates, *J. Mater. Civ. Eng.*, *14*(3), 262–269, doi:10.1061/(ASCE)0899-1561(2002)14:3(262).

Lyakhovsky, V., Y. Ben-Zion, and A. Agnon (2001), Earthquake cycle, fault zones, and seismicity patterns in a theologically layered lithosphere, *J. Geophys. Res.*, *106*(B3), 4103–4120, doi:10.1029/2000JB900218.

Meyers, M. A. (1994), *Dynamic Behavior of Materials*, Wiley-Intersci., New York, doi:10.1002/9780470172278.

Mitchell, T. M., T. Shimamoto, J. Ando, and Y. Ben-Zion (2008), The seismic velocity and permeability properties of pulverized rocks, *Geophys. Res. Abstr.*, *10*, Abstract EGU2008-A-06510.

Oglesby, D. D., R. J. Archuleta, and S. B. Nielsen (1998), Earthquakes on dipping faults: The effects of broken symmetry, *Science*, *280*(5366), 1055–1059, doi:10.1126/science.280.5366.1055.

Oglesby, D. D., R. J. Archuleta, and S. B. Nielsen (2000), Dynamics of dip-slip faulting: Explorations in two dimensions, *J. Geophys. Res.*, *105*(B6), 13,643–13,653, doi:10.1029/2000JB900055.

Power, W. L., and T. E. Tullis (1989), The relationship between slickenside surfaces in fine grained quartz and seismic cycle, *J. Struct. Geol.*, *11*(7), 879–893, doi:10.1016/0191-8141(89)90105-3.

Power, W. L., and T. E. Tullis (1995), A review of the fractal character of natural fault surfaces with implications for friction and the evolution of fault zones, in *Fractals in The Earth Sciences*, edited by C. Barton and P. Lapointe, pp. 89–105, Plenum, New York.

Power, W. L., T. E. Tullis, and J. D. Weeks (1988), Roughness and wear during brittle faulting, *J. Geophys. Res.*, *93*(B12), 15,268–15,278, doi:10.1029/JB093iB12p15268.

Prakash, V., F. Yuan, O. Dor, T. Tullis, and D. Goldsby (2008), Laboratory investigations of the origin of pulverized rocks, *Eos Trans. AGU*, *89*(53), Fall Meet. Suppl., Abstract T53F–03.

Reches, Z., and T. Dewers (2004), Gouge formation by dynamic pulverization during earthquakes, *Eos Trans. AGU*, *85*(47), Fall Meet. Suppl., Abstract S31D–01.

Reches, Z., and T. A. Dewers (2005), Gouge formation by dynamic pulverization during earthquake rupture, *Earth Planet. Sci. Lett.*, *235*(1–2), 361–374, doi:10.1016/j.epsl.2005.04.009.

Rockwell, T., M. Sisk, G. Girty, O. Dor, N. Wechsler, and Y. Ben-Zion (2009), Chemical and physical characteristics of pulverized Tejon Lookout granite adjacent to the San Andreas and Garlock faults: Implications for earthquake physics, *Pure Appl. Geophys.*, *166*(10–11), 1725–1746, doi:10.1007/s00024-009-0514-1.

Rosakis, A. (2002), Intersonic shear cracks and fault ruptures, *Adv. Phys.*, *51*(4), 1189–1257, doi:10.1080/00018730210122328.

Rosakis, A., K. Xia, G. Lykotrafitis, and H. Kanamori (2009), Dynamic shear rupture in frictional interfaces: Speeds, directionality, and modes, in *Earthquake Seismology: Treatise on Geophysics*, edited by H. Kanamori, pp. 153–192, Elsevier, Boston, Mass.

Samudrala, O., Y. Huang, and A. J. Rosakis (2002), Subsonic and intersonic shear rupture of weak planes with a velocity weakening cohesive zone, *J. Geophys. Res.*, *107*(B8), 2170, doi:10.1029/2001JB000460.

Schock, R. N., and H. C. Heard (1974), Static mechanical-properties and shock loading response of granite, *J. Geophys. Res.*, *79*(11), 1662–1666, doi:10.1029/JB079i011p01662.

Shazly, M., V. Prakash, and B. A. Lerch (2009), High strain-rate behavior of ice under uniaxial compression, *Int. J. Solids Struct.*, *46*(6), 1499–1515, doi:10.1016/j.ijsolstr.2008.11.020.

Sisk, M., T. Rockwell, G. Girty, O. Dor, and Y. Ben-Zion (2005), Potentially pulverized granites along the Garlock faults: An analysis into their physical and chemical properties, *Eos Trans. AGU*, *86*(52), Fall Meet. Suppl., Abstract S41B–0994.

Stillings, M. (2007), Structural, textural, and geochemical analyses of fault damage zones: Clark strand, San Jacinto fault zone, southern California, M.S. thesis, San Diego State Univ., San Diego, Calif.

Subhash, G., and G. Ravichandran (2000), Split-Hopkinson pressure bar testing of ceramics, in *American Society for Metals Handbook*, pp. 497–504, Am. Soc. for Metals Int., Materials Park, Ohio.

Sunny, G., F. Yuan, V. Prakash, and J. J. Lewandowski (2008), Effect of high strain rates on peak stress in a Zr-based bulk metallic glass, *J. Appl. Phys.*, *104*, 093522, doi:10.1063/1.3009962.

Templeton, E. L., and J. R. Rice (2008), Off-fault plasticity and earthquake rupture dynamics: 1. Dry materials or neglect of fluid pressure changes, *J. Geophys. Res.*, *113*, B09306, doi:10.1029/2007JB005529.

Viesca, R. C., E. L. Templeton, and J. R. Rice (2008), Off-fault plasticity and earthquake rupture dynamics: 2. Effects of fluid saturation, *J. Geophys. Res.*, *113*, B09307, doi:10.1029/2007JB005530.

Walter, W. R., and J. Brune (1993), Spectra of seismic radiation from a tensile crack, *J. Geophys. Res.*, *98*(B3), 4449–4459, doi:10.1029/92JB02414.

Wilson, B., Z. Reches, T. Dewers, and J. Brune (2004), Texture and energetics of gouge powder from earthquake rupture zones, *Eos Trans. AGU*, *85*(47), Fall Meet. Suppl., Abstract T21D–07.

Wilson, B., T. Dewers, Z. Reches, and J. Brune (2005), Particle size and energetics of gouge from earthquake rupture zones, *Nature*, *434*(7034), 749–752, doi:10.1038/nature03433.

Yuan, F., and V. Prakash (2009), Origin of pulverized rocks during co-seismic slip, paper presented at Annual Conference and Exposition on Experimental and Applied Mechanics, Soc. of Exp. Mech., Albuquerque, N. M.

Yund, R. A., M. L. Blanpied, T. E. Tullis, and J. D. Weeks (1990), Amorphous material in high strain experimental fault gouges, *J. Geophys. Res.*, *95*(B10), 15,589–15,602, doi:10.1029/JB095iB10p15589.

Zhou, Z., D.-y. Li, M. Guo-wei, and L. Jian-Chun (2008), Failure of rock under dynamic compressive loading, *J. Cent. South Univ. Technol.*, *15*, 339–343, doi:10.1007/s11771-008-0064-1.

V. Prakash and F. Yuan, Department of Mechanical and Aerospace Engineering, Case Western Reserve University, 10900 Euclid Ave., Cleveland, OH 44106-7222, USA. (vikas.prakash@case.edu; fpyuan@lnm.imech.ac.cn)

T. Tullis, Department of Geological Sciences, Brown University, Providence, RI 02912-1846, USA. (Terry_Tullis@brown.edu)